

pubs.acs.org/ac Article

Dual-Color Peak Force Infrared Microscopy

Qing Xie, Jared Wiemann, Yan Yu, and Xiaoji G. Xu*



Cite This: Anal. Chem. 2022, 94, 1425-1431



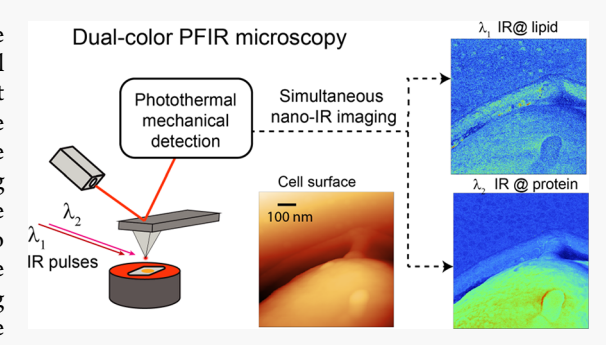
ACCESS I

Metrics & More

Article Recommendations

Supporting Information

ABSTRACT: Peak force infrared (PFIR) microscopy achieves nanoscale infrared imaging at sub-10 nm spatial resolution through photothermal mechanical detection of atomic force microscopy (AFM). However, it suffers from a major limitation that only one infrared frequency can be scanned for an AFM frame at a time. To overcome this limitation, we report here dual-color PFIR microscopy that enables simultaneous imaging at two infrared frequencies. This dual-color PFIR microscopy bypasses the limitations of frame drift and distortion of AFM when comparing two images of different infrared frequencies. We benchmark the performance and spatial resolution of this method using structured polymers exhibiting phase separation. We further demonstrate the application of this technique in imaging biological samples by mapping the cell wall of *Escherichia coli*



(E. coli) bacteria. The presence of a bacterial outer membrane was detected without extrinsic labels. This dual-color PFIR microscopy enables simultaneous nondestructive chemical nanoimaging of multiple chemical components and will be useful for potential applications such as in situ dual-channel monitoring of chemical reactions.

INTRODUCTION

Infrared (IR) radiation is directly coupled to the vibrational modes of molecules and phonon modes of crystals. IR spectroscopy—through the measurement of IR absorption—allows label-free detection of chemical compositions and is widely used in analytical chemistry. However, IR spectroscopy is limited by its spatial resolution. The long wavelength of IR radiation restricted by Abbe's diffraction limit means that the spatial resolution of IR spectroscopy and microscopy is typically a few micrometers, a scale much larger than the spatial features of many nanomaterials and biological objects. ¹

An effective and increasingly popular way to bypass Abbe's diffraction limit in IR microscopy is to utilize atomic force microscopy (AFM) together with IR radiation, either through the optical detection of near-field scattered light^{2,3} or through the mechanical detection of samples as a result of light—matter interactions.^{4–7} The detection of photothermal response by a sharp AFM tip forms the basis of the AFM-IR techniques that operate in the AFM contact mode,⁸ tapping mode,^{9–11} and peak force tapping mode.⁷ Various AFM-IR techniques have been utilized for nanoscale chemical imaging of a wide variety of materials from macromolecules such as polymers and proteins¹² and aerosols^{13,14} to polaritons in two-dimensional materials and to organic matters in rigid oil shale source rocks.^{12,15,16}

In a typical AFM-IR imaging application, images at two or more IR frequencies are collected separately to illustrate the spatial distribution of the chemical composition of interest, either revealing two different chemical compositions or showing that the IR response depends on the sample resonance. However, currently available AFM-IR techniques all suffer from one important limitation that only singlefrequency imaging is possible at a time. This means that in applications when IR imaging at multiple frequencies is required, the same area of a sample must be scanned separately and consecutively at different frequencies. This is problematic because consecutively scanned AFM images are often misaligned due to nanoscale drifts and distortions caused by hysteresis and creep of the piezoelectric scanners as well as possible thermal drift.¹⁷ This misalignment between frames can be further aggravated in atomic force microscopes, where an open-loop piezoelectric scanner is used. The frame drift and distortion problem also becomes severe in scanning submicrometer areas under ambient conditions because of large and unpredictable temperature fluctuations from the surroundings. How can this frame drift and distortion issue be bypassed in AFM-based infrared nanospectroscopy?

In this article, we address this question by developing dualcolor peak force infrared (PFIR) microscopy that, in a single AFM scan, simultaneously acquires IR images at two different frequencies. By eliminating the need for consecutive scans of the same sample area, this new configuration of PFIR microscopy bypasses the frame drift issue in AFM-IR. As a

Received: November 2, 2021 Accepted: December 20, 2021 Published: December 28, 2021





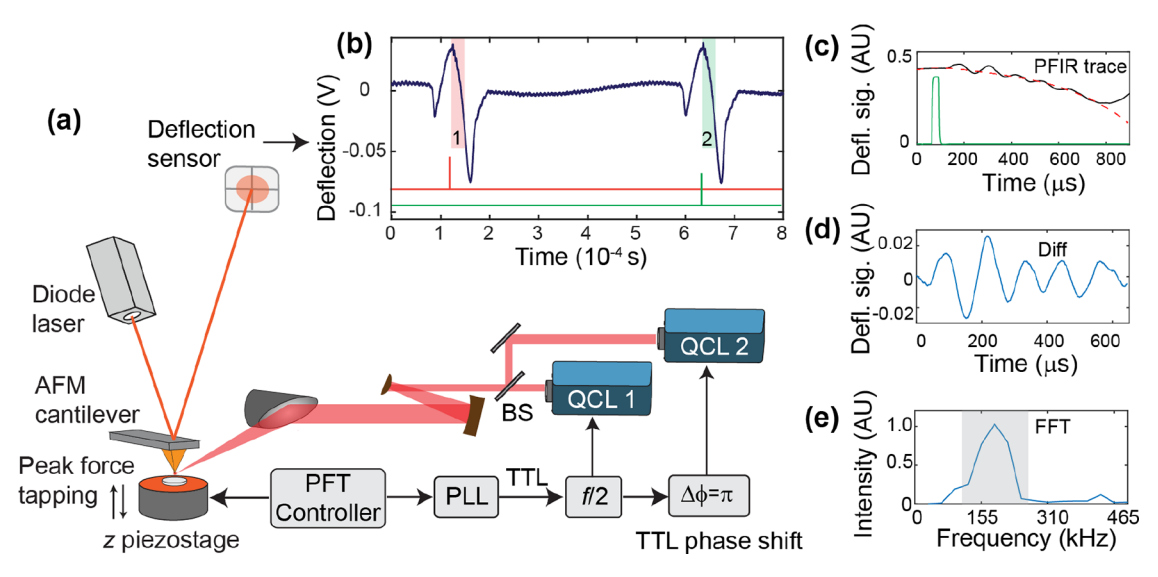


Figure 1. (a) Instrument schematics of the dual-color PFIR microscope. (b) Cantilever deflection curve of two consecutive PFT cycles. Each PFT cycle has a laser illumination from the infrared light source. Photothermal expansion of the sample leads to a mechanical response of the AFM cantilever, yielding deflection signals (highlighted by the red and green regions). (c) Zoomed-in section of the cantilever deflection trace when the tip and sample are in contact. The additional oscillations are created from the photothermal expansion of the sample. The slow varying envelope of the PFT cycle is fit with a polynomial (red dashed line) and subtracted. (d) Pure oscillation component without a slow varying envelope. (e) Fourier transform of the oscillation response in panel (d). The PFIR signal is obtained by an integration across the mechanical response peak in the frequency domain.

demonstration, we applied this new technique to measure polymer blends, block copolymers, and bacterial cell *Escherichia coli* (*E. coli*). Our measurements collectively demonstrate the capacity of the dual-color PFIR to reveal nanoscopic chemical and topographic heterogeneity in both biological and synthetic materials.

METHOD

Dual-color PFIR microscopy is a further development of PFIR microscopy that was developed by our group in 2017. PFIR microscopy is an AFM-IR technique that operates in the peak force tapping mode. The details of how to construct a PFIR microscope were described in the literature.7,12 Dual-color PFIR microscopy was developed based on the original PFIR microscopy with the integration of two frequency-tunable IR light sources and a synchronization mechanism. Figure 1a displays the schematics of a dual-color PFIR microscope. An AFM controller (Nanoscope V, Bruker) drives an atomic force microscope (Multimode 8, Bruker) to operate in the peak force tapping (PFT) mode with a peak force tapping frequency of 4 kHz. A frequency waveform that is synchronized with the PFT drive is routed to a lock-in amplifier (MFLi, Zurich Instruments) acting as a phase lock loop (PLL) and a frequency divider to generate a transistor-to-transistor logic (TTL) waveform at half of the PFT frequency. One replica of the half PFT frequency TTL waveform is used to trigger the IR pulse emission of one quantum cascade laser (QCL, MIRcat-QT, DRS Solutions); another replica of the half PFT frequency TTL waveform is phase-delayed by π and triggers the IR emission of another QCL of a similar model to emit IR pulses. The duration of the IR pulses was chosen to be a few hundred nanoseconds. The phase of the PLL is adjusted to delay the emission of the laser pulse to the moment when the tip is in dynamic contact with the sample surface in the PFT cycle. This trigger design enables the laser pulses from each QCL to illuminate the tip-sample region at every other PFT cycle. The

IR pulses from both QCLs are combined with a 1:1 beam splitter and collinearly propagate. After several steering mirrors and a beam expander, the combined beam reaches a parabolic mirror (0.25 NA) and is focused on a metal-coated AFM tip (HO:NSC 14, MikroMasch). The scan rate of the tip is set to 0.1 Hz over 256 \times 256 points for each measurement in this work. The presence of the tip-enhanced IR field of nanosecond-level duration causes a rapid photothermal expansion of the sample underneath the AFM tip, leading to mechanical excitation of the AFM cantilever, primarily at its mechanical resonances. The experimentally detected cantilever vertical deflection curve that contains the photothermal responses is plotted in Figure 1b. The radiations from each QCL illuminate the sample region alternatively for every other cycle when the tip sample is in dynamic contact. The cantilever deflection responses are sorted into two categories that correspond to each QCL illumination (Figure 1b). The slow varying background due to the PFT indentation is fitted with a fourth-order polynomial and subtracted (Figure 1c). The resulting cantilever oscillation responses (Figure 1d) undergo fast Fourier transform (FFT) to exact an oscillation amplitude and are used as the PFIR signal (Figure 1e). The PFIR signals from both IR illuminations are registered concurrently to obtain the dual-color PFIR signal. These signals are plotted with the lateral positions of the AFM tip to form images. Similar to the regular PFIR imaging operation, PFT-enabled AFM provides complementary mechanical information with the PeakForce Quantitative NanoMechanical (PFQNM) mapping capability with modulus and adhesion maps. 18

SAMPLE PREPARATIONS

The blend polymer sample composed of polystyrene (PS) and polymethyl methacrylate (PMMA) was prepared by spin-coating the 12 mg/mL (PS:PMMA = 1: 1.5) solution in toluene on a silicon substrate. The block polymer sample was made in the same way with 7.2 mg/mL PS-b-PMMA (95-b-92,

 $M_{\rm w}/M_{\rm m}=1.10$; P8537-SMMA, Polymer Source) in toluene solution. The spin-coater (KW-4A) was set to 620 revolutions per minute (rpm) for 6 s and 2800 rpm for 60 s.

To prepare E. coli samples, a frozen stock of E. coli (MG1655) was streaked onto a lysogeny broth agar plate and incubated overnight at 37 °C. Liquid cultures were then made by transferring three colonies from the agar plate into lysogeny broth and incubating the bacteria overnight at 37 °C with shaking. E. coli was subsequently washed three times with 0.85 wt % NaCl followed by three washes using 2 mM HEPES buffer containing 25 mM NaCl (pH 7.2). The E. coli suspension was allowed to adsorb onto a piranha-etched silica substrate for 2 h to allow sufficient bacterial adhesion to the substrate. After E. coli adhesion, the bacteria were fixed overnight in Karnovsky's fixative (7 wt % glutaraldehyde and 5 wt % paraformaldehyde) at 4 °C. After fixation, excess fixative was washed away with deionized water and then the samples were dehydrated sequentially by a series of 35, 50, 75, 95, and 100% ethanol washes. Samples were then washed twice with hexamethyldisilazane and air-dried in a desiccator overnight. Samples were stored in a sealed Petri dish at room temperature until use.

RESULTS

Benchmarking Dual-Color PFIR with Polymers. We first carried out the dual-color PFIR measurement with the blend polymer (PS:PMMA = 1:1.5, 12 mg/mL) as a standard sample to demonstrate our home-built experimental setup. The topography of the polymer sample is plotted in Figure 2a. Clear phase separation is observed from the height of the topography, although it is difficult to directly assign the

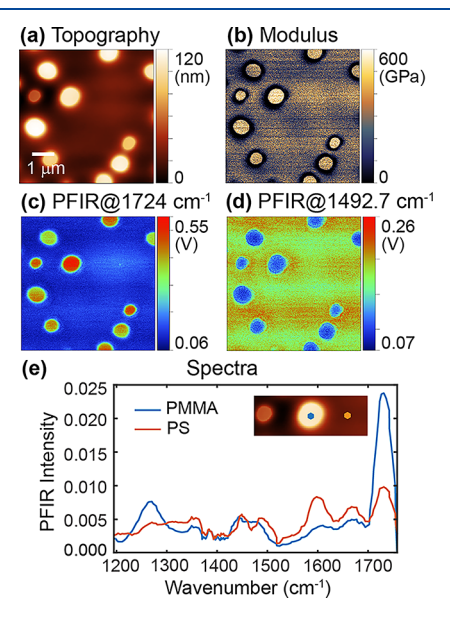


Figure 2. Dual-color PFIR imaging and spectroscopy of a PS:PMMA blend polymer film. (a, b) AFM topography and modulus of the PS:PMMA blend polymer. (c, d) Dual-color PFIR images of the PS:PMMA blend polymer at 1724 and 1492.7 cm⁻¹ under the infrared absorption of PMMA and PS, respectively. (e) PFIR spectra of the blend polymer film. The blue and orange hexagons in the inset topography are the positions for collecting the spectra of the PMMA (blue curve) and PS (orange curve) domains. The spectra are measured by the QCL with the increment of 2 cm⁻¹ and smoothed by using the Savitzky—Golay method with the degree of 2 and the span of 15. The background is removed.

chemical compositions to the domains. The modulus map of the polymer is plotted in Figure 2b. The circular domains exhibit an elevated modulus compared with the planar matrix. Note that the modulus from the PeakForce QNM corresponds to a dynamic modulus of high frequency that is different from the static modulus of the bulk measurement. Unless the two components show drastic differences in modulus, it is not reliable to use the measured modulus alone for the chemical identification for polymers. The PFIR images at corresponding IR absorption frequencies are better for chemical identifications. Figure 2c,d displays the dual-color PFIR maps at 1724 and 1492.7 cm⁻¹, respectively. The 1724 cm⁻¹ corresponds to the carbonyl vibrations of PMMA; ¹⁹ the 1492.7 cm⁻¹ corresponds to the aromatic ring bending of the PS. ²⁰ At the characteristic IR frequency of PMMA (1724 cm⁻¹), the circular domains exhibit high signals, which confirm that their chemical composition is PMMA. The planar matrix shows a higher signal at 1492.7 cm⁻¹, which corresponds to PS. Four images of Figure 2a-d were collected simultaneously in one AFM scan. After dual-color PFIR imaging, we also collected the PFIR spectra from the PMMA domain and the PS planar matrix. The spectra are displayed in Figure 2e.

We used a PS-b-PMMA block copolymer to further benchmark dual-color PFIR microscopy. A spin-coated thin film of 7.2 mg/mL block polymer PS-b-PMMA (P8537-SMMA, $M_{\rm w}/M_{\rm m}=1.10$) was measured. As Figure 3a

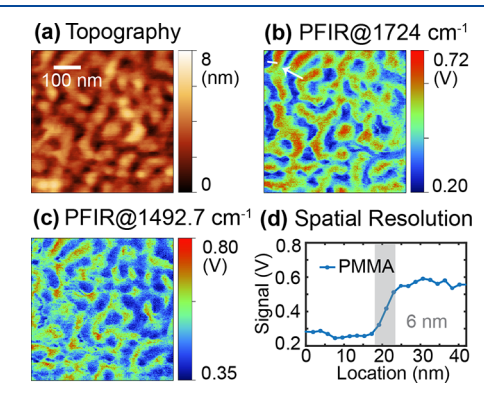


Figure 3. Dual-color PFIR of nanophase separation of a PS-*b*-PMMA block copolymer film. (a) AFM topography of the PS-*b*-PMMA block copolymer. (b, c) Dual-color PFIR images of the PS-*b*-PMMA block copolymer at 1724 and 1492.7 cm⁻¹ under the infrared absorption of PMMA and PS, respectively. (d) The spatial resolution is 6 nm estimated from the width between 10 and 90% of the edge height of the PFIR signal (gray band). The signal is extracted from the section profile marked with a white line at the upper left corner in panel (b).

illustrates, the height variation of the polymer film is less than 8 nm. Figure 3b,c shows the dual-color PFIR results mapping PMMA and PS domains in a 500 nm by 500 nm area, respectively. The PFIR images reveal the respective distributions of the PMMA and PS domains. Because both PFIR images were collected in one AFM scan, there is no relative offset or distortions between them, which is improved from typical single-frequency PFIR imaging of consecutive scans. The single-frequency PFIR scans of the block polymer at the two frequencies are shown in Figure S1 as a reference to show the drift and distortion. The spatial resolution of dual-color PFIR microscopy is estimated from a sectional profile along a white line in the IR image in Figure 3b from the IR response of PMMA at 1724 cm⁻¹. The signal versus location (nm) from

this sectional profile is shown in Figure 3d. A spatial resolution of \sim 6 nm is obtained from the width between 10 and 90% of the maximal heights of the signal at the edge. More spatial resolution estimations of \sim 6 nm from the PS channel are shown in Figure S2.

Dual-Color PFIR Imaging of *E. coli*. One important application of AFM-IR technologies is to perform label-free chemical imaging of biological samples. *E. coli* is a widely used model microorganism. To demonstrate the capability of dual-color PFIR microscopy, we mapped the cell wall composition of single *E. coli* cells that were chemically fixed and dehydrated on a silica substrate. To avoid the collapse and shrinkage of *E. coli* cells, samples were carefully dehydrated following the protocol of biological sample preparations for scanning electron microscopy. Prom topography imaging in Figure 4a, we observed that the *E. coli* cell has a rod shape of

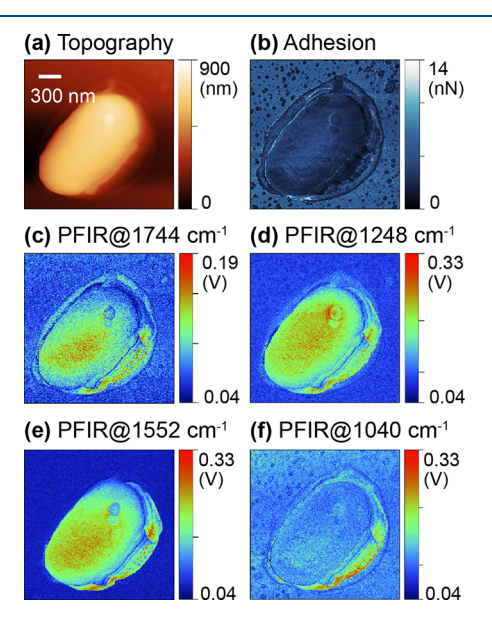


Figure 4. Dual-color PFIR imaging of an *E. coli*: bacterium. (a, b) AFM topography and adhesion of *E. coli*. (c, d) Dual-color PFIR images of *E. coli* at 1744 and 1248 cm⁻¹ corresponding to the infrared absorption of lipids and amide III, respectively. (e, f) Dual-color PFIR images of *E. coli* at 1552 and 1040 cm⁻¹, corresponding to infrared absorption of amide II and nucleic acids, respectively. Panels (c) and (d) and panels (e) and (f) are the two individual dual-color PFIR measurements.

approximately 0.9 μ m in width and 1.7 μ m in length. For PFIR imaging, we first acquired dual-color images of E. coli simultaneously at 1744 and 1248 cm⁻¹ shown in Figure 4c,d, respectively. We chose these two frequencies because they correspond to IR signals from fatty acids and amide III region associated with proteins and peptides, all of which are key components of the E. coli cell wall. Specifically, infrared signals at 1700-1800 cm⁻¹ are characteristic of fatty acid esters and phospholipids, and several frequencies between 1180 and 1300 cm⁻¹ indicate the broadly defined amide III region associated with proteins and peptides.²³ A peak at 1743 cm⁻¹ has been previously identified as C=O stretch of phospholipids,²⁴ while a peak at 1248 cm⁻¹ has generally been assigned to an unspecified, characteristic vibration of amides.²⁵ We then simultaneously acquired images at 1552 and 1040 cm⁻¹ (Figure 4e,f). The peak measured at 1552 cm⁻¹ falls within the amide II spectral range. The 1040 cm⁻¹ frequency falls

within the spectral range of polysaccharides but may also correspond to DNA and RNA phosphate stretches (1040–1100 cm⁻¹).²⁵ The PFIR images revealed that most of the bacterial cell surface strongly adsorbs at 1744, 1248, and 1552 cm⁻¹ frequencies compared to the bare substrate but weakly at 1040 cm⁻¹. These strong adsorption signals indicate the predominant presence of fatty acids, membrane proteins, and lipopolysaccharide, which are known main components of the *E. coli* outer membrane.²⁶

Meanwhile, we observed two intriguing features of the E. coli surface. One is a ring structure closely surrounding the rodshaped bacterial cell. The adhesion and topographical images revealed that this ring structure is ~130 nm in width and ~28 nm in height (detailed characterization in Figure S3). The chemical composition of this ring structure is quite complex and non-uniform, as indicated by the non-uniform distribution of IR signals. Some portion of the ring structure has strong absorbance in 1744 cm⁻¹, which suggests enrichment of fatty acid esters and phospholipids. In contrast, some other portion of the ring structure has strong absorbance at all four frequencies, which suggests a complex mixture of possible polysaccharides, proteins, lipids, and nucleic acids. Interestingly, similar ring structures were shown before for E. coli in AFM studies, but the origin of such a structure was not identified.²⁷ It is clear from our PFIR images that this extra layer of materials covering the E. coli cell has a heterogeneous and complex composition. We speculate that its formation might be related with the bacterial adhesion to the substrate, as E. coli is known to secrete an extrapolymer matrix, which includes polysaccharides, proteins, lipids, and DNA, to form biofilms.²⁸ A second intriguing feature we observed is a small, spherical protrusion on the E. coli surface. It was roughly 100 nm in diameter, estimated from topographical mapping. The PFIR spectral scan revealed that this protrusion has much weaker IR signals at 1744 and 1552 cm⁻¹ than the remaining surface of the bacterial cell. This indicates that this unknown protrusion has a unique surface chemistry and is possibly not enriched in membrane proteins. The identity of this protrusion is unclear and needs further investigation.

To further study *E. coli* with dual-color PFIR microscopy, we performed zoomed-in scans to reveal additional details of chemical distributions on the E. coli surface, of the ring structure, and of the cell protrusion (Figure 5). The AFM topography acquired during two separate dual-color PFIR scanning clearly showed the ring structure surrounding the E. coli cell (Figure 5a,d). Figure 5a,d shows sequentially acquired images of the same area of the sample. The small difference in the morphology is due to the inevitable instrumental drift between two scans. This further highlights the importance of simultaneous dual-color PFIR imaging when comparing signals from multiple frequencies. By performing zoomed-in PFIR imaging (2.5 times) at 1744 and 1248 cm $^{-1}$ (Figure 5b,c), we observed a similar but more detailed chemical profile than that in Figure 4. It is evident that the cell surface, its surrounding ring structure, and the protrusion all have distinctly different adsorption at different frequencies, which indicates their heterogeneous chemical compositions. We next performed a dual-color PFIR scan at 1644 and 1016 cm⁻¹. The 1644 cm⁻¹ frequency is within the amide I frequency (1630–1700 cm⁻¹), whereas the 1016 cm⁻¹ frequency has previously been assigned to the C-O stretch of polysaccharides, although many other biomolecules also adsorb in this region. 23,25 Similar to the amide II frequency measured in Figure 4e, we observed a

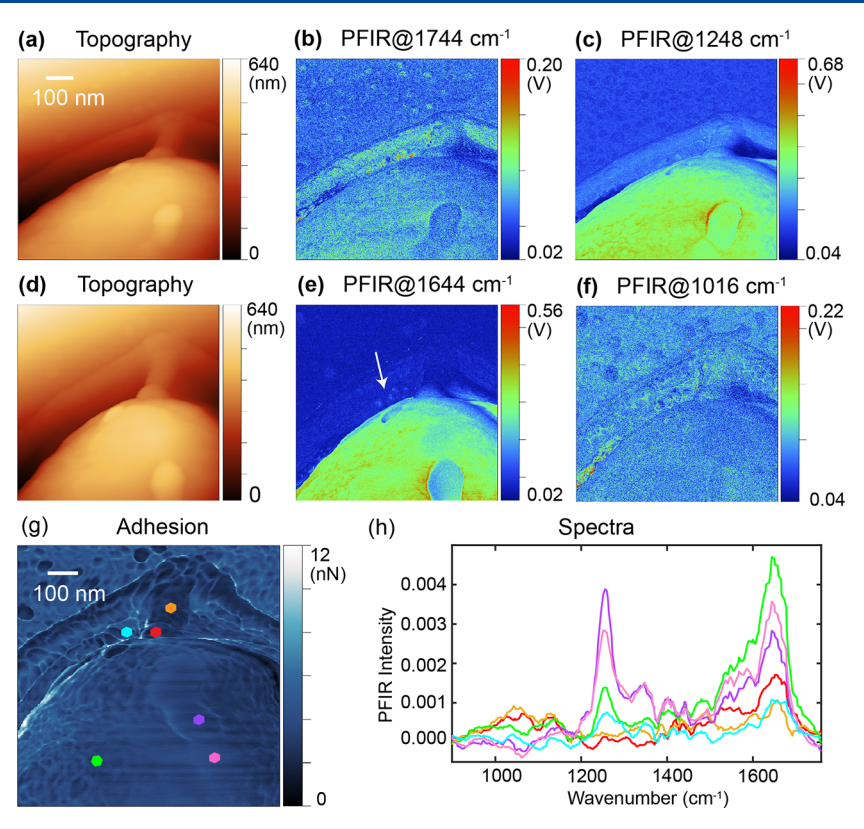


Figure 5. Dual-color PFIR imaging and spectroscopy on a part of the *E. coli* bacteria. (a, d) AFM topography of a part of the *E. coli* bacteria. (b, c) Dual-color PFIR images of the part of *E. coli* bacteria at 1744 and 1248 cm⁻¹ under the infrared absorption of lipids and amide III, respectively. (e, f) Dual-color PFIR images of the part of *E. coli* bacteria at 1644 and 1016 cm⁻¹ under the infrared absorption of amide I and sugars, respectively. (g) Adhesion of the part of the *E. coli* bacteria. (h) PFIR spectra of six positions of the part of the *E. coli* bacteria in panel (g). The background is removed. The spectra are measured by the QCL with the increment of 2 cm⁻¹ and smoothed by using the Savitzky–Golay method with the degree of 2 and the span of 15. Panels (a)–(c) and panels (d)–(f) are from two groups of dual-color PFIR measurements.

strong absorption of 1644 cm⁻¹ on the *E. coli* surface with weaker absorption on the protrusion shown in Figure 5e. Simultaneous measurement at 1016 cm⁻¹ in Figure 5f revealed that the bacterial cell surface has low absorption at this frequency, even though there were a few nanosized "hotspots" within the ring structure with slightly higher signals. The outer membrane of Gram-negative bacteria is generally covered by lipopolysaccharides with long sugar chains, referred to as Oantigens. However, the strain (MG1655) studied here contains a mutation that prevents the biosynthesis of O-antigen, which explains the relatively low absorbance at 1016 cm⁻¹ on the bacteria surface.²⁹

In addition to acquiring dual-color PFIR images, we also measured the point spectra at different locations on the E. coli sample. The point spectra can be used to elucidate chemical heterogeneity at different locations on the surface of a sample by sweeping a range of IR frequencies. In the adhesion map of the E. coli sample (Figure 5g), six colored points were used to indicate the six locations where the PFIR spectra (coded with the same color in Figure 5h) were acquired. From the point spectra, we found that the cell surface (green-colored spectrum) is highly enriched with amide I, as indicated by the strong signal peak at 1644 cm⁻¹. In contrast, the cell surface protrusion (purple and pink) has significantly stronger absorptions around 1256 cm⁻¹ but a slightly weaker signal at 1644 cm⁻¹. This suggests that the protrusion is more enriched with amide III. These findings emphasize the capabilities of the dual-color PFIR technique to investigate nanoscale heterogeneity on biological samples.

DISCUSSION

One advantage of dual-color PFIR microscopy stems from the need to bypass the presence of AFM drift in comparing two nanoscale IR images taken consecutively. The consecutive scans of the AFM frames can drift due to environmental temperature fluctuations; the scale of the scan can be distorted due to the hysteresis and creep of piezo materials of the AFM scanner.³⁰ In the case of an atomic force microscope with an open-loop scanner, the majority of the frame drift and distortions are not compensated. In the case of a nonsparse sample of a small region filled with tiny features, the side-byside comparison of two chemical images from different scan frames is difficult without ad hoc frame compensation. In our experimental apparatus, we used the Multimode 8 atomic force microscope, which is an open-loop atomic force microscope that inevitably suffers from the creep of the piezo scanner. Dual-color PFIR microscopy bypasses the limitation of the piezo scanner creep, hysteresis, and temperature fluctuations in comparing two nano-IR images at two frequencies. The other advantage of dual-color PFIR microscopy is the doubled measurement speed—two IR frames can be obtained simultaneously, albeit with a slightly reduced signal-to-noise ratio.

On the basis of dual-color PFIR operation, the implementation of more QCLs to further expand the number of interleaving IR frequencies is doable. Such a capability would permit simultaneously tracking three or more chemical compositions in one AFM scan to achieve multiplex nano-IR capability. In building such multiplex PFIR apparatus, we

recommend using suitable IR dichroic long-wave pass or short-wave pass filters to avoid power loss when combining multiple IR beams of different frequencies.

With the dual-color PFIR technique, we have chemically mapped a biological sample of *E. coli* on the silica substrate. Topographical and adhesion mapping revealed a spherical protrusion on the *E. coli* surface and a ring content surrounding the bacteria. Simultaneous acquisition of IR images supplied contrast between the spherical protrusion and the bacterial surface due to the unique chemical makeup of the two surfaces. A deeper investigation is needed to identify the protrusion, but these results demonstrate the utility of dual-color PFIR to study nanoscale chemical and morphological heterogeneity on cell surfaces.

As an outlook, the potential application of the detection mechanism of dual-color PFIR microscopy is to track in situ chemical reactions. For example, one of the IR wavelengths can be chosen to match the vibrational signatures of the reactant molecules and the other IR wavelength to match that of the product molecules. The disappearance and emergence of the reactant and the product can be imaged simultaneously at the nanoscale. In addition, the same dual-color PFIR detection principle can be applied to the recently developed liquid-phase peak force infrared microscopy³¹ to track slow reorganization processes in liquid environments. Moreover, the dual-color implementation of PFIR microscopy can operate to accommodate an internal reference to the spectroscopic response at different frequencies: fixing one of the IR pulses at a nonresonant frequency and adjusting the other IR frequency to resonances of interest. In such an implementation, the nonresonant photothermal response could be used as a subtractable background to remove the nonresonant photothermal residual signal to extract the photothermal signal proportional to the sample's IR absorption.

CONCLUSIONS

In summary, we have developed dual-color PFIR microscopy that allows simultaneous nanoscale chemical imaging with two independent IR frequencies, which bypasses the frame drift issue in AFM-based IR microscopy. In addition, we demonstrated dual-color PFIR microscopy on nanostructured polymers and biological cells, resolving multiple compositions in nanoscale heterogeneous samples. As an outlook, dual-color PFIR microscopy will serve as a suitable platform for tracking slow chemical reactions at the interface and removing nonresonant photothermal backgrounds in AFM-based IR microscopy.

ASSOCIATED CONTENT

Solution Supporting Information

The Supporting Information is available free of charge at https://pubs.acs.org/doi/10.1021/acs.analchem.1c04756.

Two single-frequency PFIR scans of a PS-b-PMMA block polymer thin film (Figure S1); spatial resolution of dual-color PFIR (Figure S2); height and width of the outer membrane of *E. coli* bacteria from topography (Figure S3) (PDF)

AUTHOR INFORMATION

Corresponding Author

Xiaoji G. Xu — Department of Chemistry, Lehigh University, Bethlehem, Pennsylvania 18015, United States; o orcid.org/0000-0003-0847-5871; Email: xgx214@lehigh.edu

Authors

Qing Xie — Department of Chemistry, Lehigh University, Bethlehem, Pennsylvania 18015, United States

Jared Wiemann — Department of Chemistry, Indiana
University, Bloomington, Indiana 47405, United States

Yan Yu — Department of Chemistry, Indiana University,
Bloomington, Indiana 47405, United States; orcid.org/
0000-0001-6496-5045

Complete contact information is available at: https://pubs.acs.org/10.1021/acs.analchem.1c04756

Notes

The authors declare no competing financial interest.

ACKNOWLEDGMENTS

X.G.X. would like to thank the support from Beckman Young Investigator Award from the Arnold and Mabel Beckman Foundation and the Sloan Research Fellowship from the Alfred P. Sloan Foundation. Q.X. and X.G.X. would also like to thank the support from the National Science Foundation, award number CHE 1847765. J.W. and Y.Y. acknowledge support from the National Science Foundation under award number 1705384 to Y.Y. X.G.X. would like to thank Dr. Chanmin Su for the suggestions on the applications of dual-color PFIR microscopy. Finally, Q.X. would like to thank the suggestions from Dr. Haomin Wang on writing the manuscript.

REFERENCES

- (1) Abbe, E. Archiv für mikroskopische Anatomie 1873, 9, 413-468.
- (2) Novotny, L.; Hecht, B. *Principles of Nano-Optics*; 2 ed.; Cambridge University Press: Cambridge, 2012.
- (3) Bachelot, R.; Gleyzes, P.; Boccara, A. C. Opt. Lett. 1995, 20, 1924-1926.
- (4) Anderson, M. S. Appl. Spectrosc. 2000, 54, 349-352.
- (5) Kurouski, D.; Dazzi, A.; Zenobi, R.; Centrone, A. Chem. Soc. Rev. **2020**, 49, 3315–3347.
- (6) Nowak, D.; Morrison, W.; Wickramasinghe, H. K.; Jahng, J.; Potma, E.; Wan, L.; Ruiz, R.; Albrecht, T. R.; Schmidt, K.; Frommer, J.; Sanders, D. P.; Park, S. Sci. Adv. 2016, 2, No. e1501571.
- (7) Wang, L.; Wang, H.; Wagner, M.; Yan, Y.; Jakob, D. S.; Xu, X. G. Sci. Adv. 2017, 3, No. e1700255.
- (8) Dazzi, A.; Prazeres, R.; Glotin, F.; Ortega, J. M. Opt. Lett. 2005, 30, 2388-2390.
- (9) Jahng, J.; Potma, E. O.; Lee, E. S. Anal. Chem. 2018, 90, 11054–11061.
- (10) Wieland, K.; Ramer, G.; Weiss, V. U.; Allmaier, G.; Lendl, B.; Centrone, A. *Nano Res.* **2019**, *12*, 197–203.
- (11) Mathurin, J.; Pancani, E.; Deniset-Besseau, A.; Kjoller, K.; Prater, C. B.; Gref, R.; Dazzi, A. Analyst 2018, 143, 5940-5949.
- (12) Wang, L.; Wagner, M.; Wang, H.; Pau-Sanchez, S.; Li, J.; Edgar, J. H.; Xu, X. G. Adv. Opt. Mater. 2020, 8, 1901084.
- (13) Bondy, A. L.; Kirpes, R. M.; Merzel, R. L.; Pratt, K. A.; Banaszak Holl, M. M.; Ault, A. P. *Anal. Chem.* **2017**, 89, 8594–8598. (14) Wang, L.; Huang, D.; Chan, C. K.; Li, Y. J.; Xu, X. G. *Chem. Commun.* **2017**, 53, 7397–7400.
- (15) Jakob, D. S.; Wang, L.; Wang, H.; Xu, X. G. Anal. Chem. 2019, 91, 8883–8890.

- (16) Ambrosio, A.; Jauregui, L. A.; Dai, S.; Chaudhary, K.; Tamagnone, M.; Fogler, M. M.; Basov, D. N.; Capasso, F.; Kim, P.; Wilson, W. L. *ACS Nano* **2017**, *11*, 8741–8746.
- (17) Voigtländer, B., Voigtländer, B., Artifacts in AFM. In *Atomic Force Microscopy*; Voigtländer, B., Ed. Springer International Publishing: Cham, 2019; pp. 137–147.
- (18) Pittenger, B.; Erina, N.; Su, C. Appl. Note Veeco Instrum. Inc. 2010, 1, 1-11.
- (19) Nagai, H. J. Appl. Polym. Sci. 1963, 7, 1697-1714.
- (20) Liang, C. Y.; Krimm, S. J. Polym. Sci. 1958, 27, 241-254.
- (21) Joseph, B. C.; Pichaimuthu, S.; Srimeenakshi, S.; Murthy, M.; Selvakumar, K.; Ganesan, M.; Manjunath, S. R. J. Cell Sci. Ther. 2015, 06, 221.
- (22) Bhattacharya, R.; Saha, S.; Kostina, O.; Muravnik, L.; Mitra, A. Appl. Microsc. 2020, 50, 15.
- (23) Salman, A.; Sharaha, U.; Rodriguez-Diaz, E.; Shufan, E.; Riesenberg, K.; Bigio, I. J.; Huleihel, M. *Analyst* **2017**, *142*, 2136–2144.
- (24) Sukuta, S.; Bruch, R. Lasers Surg. Med. 1999, 24, 382-388.
- (25) Movasaghi, Z.; Rehman, S.; Ur Rehman, D. I. Appl. Spectrosc. Rev. 2008, 43, 134-179.
- (26) Nikaido, H. Microbiol. Mol. Biol. Rev. 2003, 67, 593-656.
- (27) Liu, S.; Wang, Y. Scanning 2010, 32, 61-73.
- (28) Flemming, H.-C.; Wingender, J.; Szewzyk, U.; Steinberg, P.; Rice, S. A.; Kjelleberg, S. Nat. Rev. Microbiol. 2016, 14, 563-575.
- (29) Liu, D.; Reeves, P. R. Microbiology 1994, 140, 49-57.
- (30) Habibullah, H. Measurement 2020, 159, 107776.
- (31) Wang, H.; González-Fialkowski, J. M.; Li, W.; Xie, Q.; Yu, Y.; Xu, X. G. Anal. Chem. 2021, 93, 3567–3575.

☐ Recommended by ACS

Polarity Nano-Mapping of Polymer Film Using Spectrally Resolved Super-Resolution Imaging

Yejin Park, Doory Kim, et al.

SEPTEMBER 14, 2022

ACS APPLIED MATERIALS & INTERFACES

READ 🗹

Macromolecular Orientation in Biological Tissues Using a Four-Polarization Method in FT-IR Imaging

Paulina Koziol, Tomasz P. Wrobel, et al.

AUGUST 27, 2020

ANALYTICAL CHEMISTRY

READ 🗹

Nanodiffraction Imaging of Polymer Crystals

Shusuke Kanomi, Hiroshi Jinnai, et al.

JUNE 23, 2021

MACROMOLECULES

READ 🗹

Speeding up the Topography Imaging of Atomic Force Microscopy by Convolutional Neural Network

Peng Zheng, Songyuan Ding, et al.

MARCH 16, 2022

ANALYTICAL CHEMISTRY

READ 🗹

Get More Suggestions >